Topological Anderson insulator via disorder-recovered average symmetry

Jie Zhang,[1] Zhi-Qiang Zhang,[1] Shu-guang Cheng [2,*] and Hua Jiang [1,3,†]

[1]*School of Physical Science and Technology, Soochow University, Suzhou, 215006, China*
[2]*Department of Physics, Northwest University, Xi'an 710069, China*
[3]*Institute for Advanced Study, Soochow University, Suzhou 215006, China*

We propose that the topological Anderson insulator (TAI) can be realized by introducing special disorder into a graphene with a modified Kane-Mele model. The disorder recovers symmetry under statistical averaging, which turns a trivial insulator into a topologically nontrivial insulator. When graphene is subjected to nonmagnetic adatoms in one sublattice or global uniform magnetic adatoms, the sublattice or time-reversal (TR) symmetry is broken, respectively, making the system topologically trivial. For the former one, randomly spatial distributed adatoms result in gapless edge states and quantized transport characteristics. Such randomization preserves the sublattice symmetry on average and the system becomes a TAI phase. For the latter one, the average TR symmetry is recovered by randomizing magnetization directions and the topological phase is protected. We demonstrate the existence of gapless edge states, but the differential conductance is no longer quantized. Moreover, we construct our proposal in electric circuits and observe the disorder-induced edge state through the circuit simulation. Our work provides a more simplified scheme to realize the TAI, and deepens the understanding of the relationship between the TAI and average symmetries.

I. INTRODUCTION

Disorder effects of electrons as one of the most important research fields in condensed matter physics have attracted significant interest [1–12]. The interplay between disorder effects and topology leads to the discovery of topological Anderson insulators (TAIs) [13–18], where a trivial insulator gives rise to the topological features when disorder is considered. Since the early studies in HgTe/CdTe quantum wells [19,20], TAIs are reported to be realizable and detectable in a variety of topological systems [21–40]. In general, TAIs in different systems are characterized by distinct topological invariants and exhibit corresponding peculiar transport properties. Due to these differences, TAIs are also regarded to be restricted to distinct symmetries. For example, the higher-order topological Anderson insulators could demand the satisfaction of corresponding point group symmetry [22–24]. For the winding number protected TAI, its realization strongly depends on the chiral or particle-hole symmetries, among which the disorder is restricted to ensure the symmetry [25–27]. Very recently, TAIs with different symmetries are reported to be experimentally realized in cold atoms [28], photonic crystals [29,30], LC circuits [23], photonic quantum walks [38], etc.

Nevertheless, previous TAI studies mainly concentrate on both the global and local symmetry of the disordered samples, where the disorder should enforce the symmetry everywhere to preserve the nontrivial topological features,

i.e., the existence of edge states or the quantized transport properties [13,14]. More importantly, the realization of the TAI for these studies is also restricted to the on-site or hopping energy type of disorder [17,23,34–36], and the TAI is obtained by tuning the strength of random energy [41].

Compared with clean samples, the disordered samples could capture the additional symmetries under statistical averaging. Disorder breaks the local symmetry, but the global symmetry can still be maintained on statistical averaging [40,42]. Significantly, the symmetry under statistical averaging is more realistic and easier to be realized than the previously studied enforced symmetries in not only disordered classical wave systems but also condensed matter systems. However, the influence of such a symmetry, named as average symmetry, on the TAIs is rarely reported. Therefore, it is of great value to study the interplay of the TAI and average symmetries.

In this paper we present a feasible scheme to obtain the TAI via the disorder-recovered average symmetry. The physical pictures are illustrated in Fig. 1. In a clean sample [see Fig. 1(a)] the potentials represented by the peaks only distribute in the gray regions. Consequently, the gray and white regions are unequal, and the symmetry of the system is destroyed. It is a trivial insulator in which the electrons are localized. In contrast, we randomize the position of distributed peaks until the number of peaks in the gray and white regions is balanced, as in the case shown in Fig. 1(b). It is such randomization that leads to the introduction of disorder, which can hold the symmetry of the system on average, although the symmetry is still broken locally. The topological state can be restored with electrons propagating along the boundaries. We uncover that such pictures can be realized by studying

---

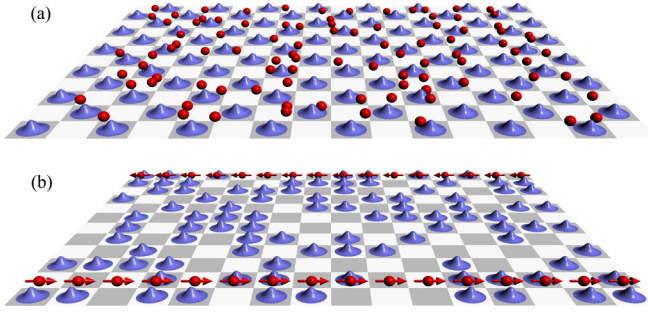*sgcheng@nwu.edu.cn
†jianghuaphy@suda.edu.cn

FIG. 1. The schematic diagrams for two different potential configurations, with peaks representing potentials. (a) The peaks are only distributed in the gray regions, making the gray and white regions different. The symmetry of the system is broken and the electrons (red balls) are localized. (b) The distribution of peaks is random, and they are equally distributed on the gray and white regions. These randomly distributed peaks (disorder) make the gray and white regions equivalent under statistical averaging, although locally unequal. The symmetry of the system is restored on average with edge states along the boundaries.

both nonmagnetic and magnetic atom adsorption effects in a modified Kane-Mele model. From the numerical calculation results of differential conductance, local density of states (LDOS) and local current distributions, the emergency of the TAI phase induced by disorder-recovered average symmetry is identified. Since there is no need for the manipulation of disorder strength, finally we demonstrate that such TAI phase is much easier to be realized in classic LC circuits.

The rest of this paper is organized as follows: In Sec. II we introduce the modified Kane-Mele model with distributed adatoms and present the numerical methods. In Sec. III we concentrate on the realization of the TAI via average sublattice symmetry. The average TR symmetry-protected TAI is studied in Sec. IV. In Sec. V, a feasible scheme is presented to realize the proposal in LC circuits. Finally, a brief summary is given in Sec. VI.

II. MODELS AND NUMERICAL METHODS

We start from a modified Kane-Mele model in the presence of distributed adatoms. Two different types of adatoms are considered. We first study that graphene is adsorbed with nonmagnetic atoms, which can generate a fixed on-site energy on each influenced carbon atom [see Figs. 2(a) and 2(c)]. In the tight-binding representation, the effective Hamiltonian is [43–46]

$$H_1 = t_1 \sum_{\langle ij \rangle} c_i^\dagger c_j + it_2 \sum_{\langle\langle ij \rangle\rangle} v_{ij} c_i^\dagger s_z c_j + U \sum_{i \in \kappa} c_i^\dagger c_i, \quad (1)$$

where $c_i^\dagger$ (c_i) is the creation (annihilation) operator of an electron at site i, and $\langle ij \rangle$ and $\langle\langle ij \rangle\rangle$ mean the sum over all the nearest-neighbor (NN) and next-nearest-neighbor (NNN) hopping sites, respectively. The first term is the NN hopping with an amplitude of t_1, which acts as the energy unit. The second term describes the intrinsic spin-orbit interaction with strength t_2, where $s = (s_x, s_y, s_z)$ is the Pauli operator, and v_{ij} is defined as $v_{ij} = \frac{\mathbf{d}_i \times \mathbf{d}_j}{|\mathbf{d}_i \times \mathbf{d}_j|} = +1 \, (-1)$ when the NNN hopping
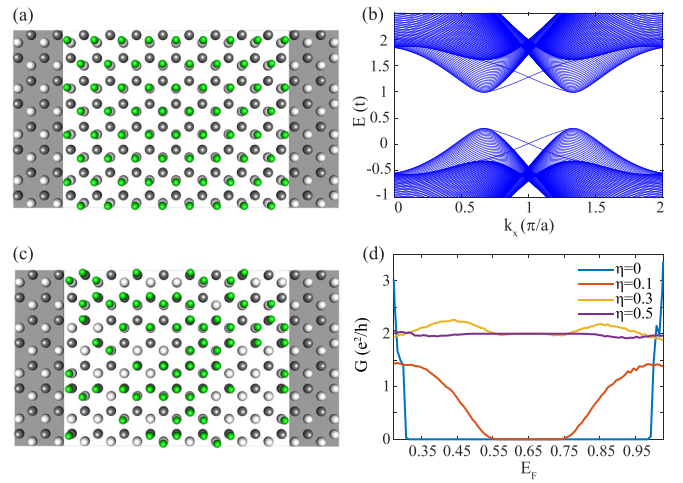

FIG. 2. (a) and (c) Schematic diagrams for the two-terminal devices with $\eta = 0$ and $\eta = 0.5$, respectively. η is the probability of distributed adatoms (green balls) on A sites, and the adatoms only exist in the central region. (b) The band structure for the central region of device (a). (d) The differential conductance G as a function of Fermi energy E_F for different η. The parameters are set to $t_1 = 1$, $t_2 = 0.06$, and $U = 1.3$. The sample size is $N = 40$, $L_x = 80$.

is counterclockwise (clockwise) with respect to the positive z axis. The third term represents the on-site energy U, which apply on the influenced sites denoted by κ.

The other type is magnetic adatoms, where a planar magnetization is produced on each site [see Figs. 4(a) and 4(c)]. The corresponding tight-binding Hamiltonian is written as [43]

$$H_2 = t_1 \sum_{\langle ij \rangle} c_i^\dagger c_j + it_2 \sum_{\langle\langle ij \rangle\rangle} v_{ij} c_i^\dagger s_z c_j + \lambda \sum_i c_i^\dagger \mathbf{B} \cdot \mathbf{s} c_i, \quad (2)$$

where the last term is the exchange field with a strength of λ.

In order to investigate how disorder affects the topological properties of the above systems, we calculate the differential conductance based on the nonequilibrium Green's function method [47,48]. Considering a sample with two semi-infinite leads [see Fig. 2(a)], the two-terminal differential conductance is calculated by $G(E) = \frac{e^2}{h} \text{Tr}(\Gamma_L G^r \Gamma_R G^a)$, where $\Gamma_\alpha = i[\Sigma_\alpha^r - (\Sigma_\alpha^r)^\dagger]$ is the linewidth function of lead α ($\alpha = L/R$). Σ_α^r is the self-energy caused by the coupling between the central region and α lead. G^r (G^a) is the retarded (advanced) Green's function, which is calculated by $G^r(E) = (EI - H_c - \Sigma_L^r - \Sigma_R^r)^{-1}$, and H_c is the Hamiltonian of the central region. In addition, several methods including LDOS and the spatial distribution of local currents are also effective ways to clarify the influence of disorder, and they are also available by the nonequilibrium Green's function method. The LDOS at a given site i is [49]

$$\rho_i(E) = -\frac{1}{\pi} \text{Im} G^r(i, i; E). \quad (3)$$

By applying a small external bias $V = V_L - V_R$ between the two terminals, the local current between the neighboring sites i and j can be expressed as [14,50]

$$J_{i \to j} = \frac{2e^2 V}{h} \text{Im}[H_{ij}(G^r \Gamma_L G^a)_{ji}]. \quad (4)$$

III. TOPOLOGICAL ANDERSON INSULATOR VIA AVERAGE SUBLATTICE SYMMETRY

We first focus on the sample with spatially distributed nonmagnetic adatoms. In Fig. 2(a), when the adatoms (green balls) are absent, the system is a quantum spin Hall (QSH) state with a pair of helical edge states inside the band gap [43]. Then we introduce the adatoms into the system and the on-site energy of the influenced carbon atom is shifted to U. It is worth noting that instead of choosing all the sites, we select half of them. Considering the limiting case, the adatoms are distributed on one sublattice of graphene. For example, they are only distributed on the atoms from B sublattice in the central region of Fig. 2(a). The corresponding energy spectrum of such a system is calculated with periodic and open boundary conditions in x and y directions, respectively. Since the adatoms only exist in one sublattice, the A/B sublattice symmetry is broken, resembling the picture of Fig. 1(a). It can be confirmed that the original edge modes are gapped out, producing a trivial insulator shown in Fig. 2(b).

For convenience, a ratio η is defined as $\eta = N_A/N_0$, where N_A is the number of adatoms on A sites and N_0 is the total number of adsorbates. That is to say, η is the probability of adatoms on A sites, and thus Figs. 2(a) and 2(b) correspond to the case $\eta = 0$. Then we randomize the adsorption sites, making η gradually increase. When the adatoms are equally distributed on A/B sites, that is $\eta = 0.5$ [see Fig. 2(c)], the sublattice symmetry has also been restored on average, resembling the picture of Fig. 1(b).

We next study the transport properties of the system. The differential conductance G is averaged over up to 1000 random configurations. Figure 2(d) shows the G versus Fermi energy E_F for different η. In the clean sample ($\eta = 0$), a trivial insulator with $G = 0$ is obtained (see the blue solid line), which is consistent with the band structure in Fig. 2(b). With the increase of η, it can be seen that the energy range with $G = 0$ is shrinking, indicating the presence of states within the original gap. When $\eta = 0.5$, as plotted in the purple solid line, a quantized conductance plateau appears with the value $G = 2e^2/h$. The existence of a quantized plateau suggests that the sample has turned into a topological insulator.

In order to further investigate the topological properties of the system, we calculate the spatial distribution of the LDOS for different η. Since the sample is connected to the metallic leads, the states of the leads will permeate into the central region. The LDOS of the regions in contact with the leads with a width of 10 is not shown. The upper panels of Fig. 3 exhibit the evolution of LDOS with η, manifesting the appearance of the edge states. For example, in the clean limit, no state is seen for energy inside the gap, where a trivial insulator is expected in Fig. 3(a). In the case of $\eta = 0.3$, as seen in Fig. 3(b), the subgap states appear in the whole region and there are more states near the boundaries. In Fig. 3(c), for $\eta = 0.5$, the disorder distribution of adatoms is enhanced and all the states tend to travel at the boundaries of the sample. Then we calculate the corresponding local current distributions $J_x(y)$ of the sample along the y direction, as illustrated in Fig. 3(d). As expected, when $\eta = 0$, there is no current. With the increase of η, the local currents appear. The local currents at $\eta = 0.5$ are much more localized to the sample boundaries than those at $\eta = 0.3$.
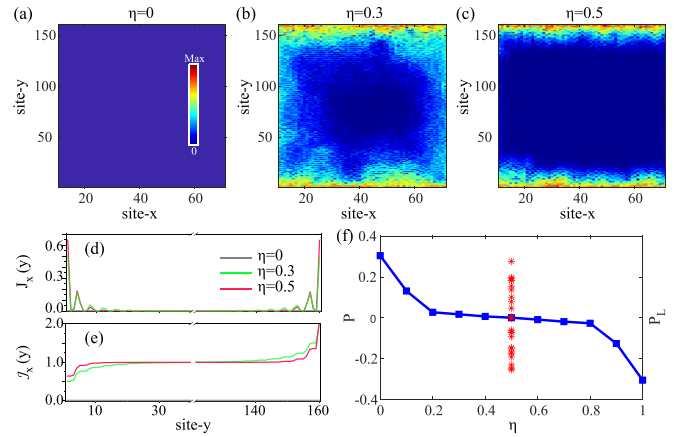

FIG. 3. The upper panels exhibit the LDOS of the system with (a) $\eta = 0$, (b) $\eta = 0.3$, and (c) $\eta = 0.5$. (d) and (e) Local current distributions $J_x(y)$ and the summation of local current distributions $\mathcal{J}_x(y)$ along the y direction under different η, respectively. (f) The evolution of P with the increase of η. The red stars are local P_L for 20 random pairs of adjacent A and B sites when $\eta = 0.5$. Here the Fermi energy is $E_F = 0.65$, and the other parameters are the same as those in Fig. 2.

Besides, the summation of the local currents from the bottom to site y, $\mathcal{J}_x(y) = \sum_{i=1}^{y} J_x(i)$, are also plotted in Fig. 3(e). One can see that the summation is about $2e^2V/h$ when $\eta = 0.5$, which means a differential conductance of $2e^2/h$, indicating that the quantized conductance is mostly contributed by the topological edge states. This result strongly manifests that the present disordered system belongs to the QSH phase.

In the above investigations we do not turn the strength of disorder. From $\eta = 0$ to $\eta = 0.5$, the on-site energy U of the adatoms is unchanged, only the adsorption positions have been changed, which is different from the conventional TAIs. Thus, the origin of the edge states is quite intriguing. At the beginning, the adatoms only distribute on the B sublattice, and the symmetry of the A/B sublattice is broken. Then with the increase of η, the average A/B sublattice symmetry is slowly restored. When $\eta = 0.5$, since the number of adatoms distributed on the A/B sublattice is the same, A and B sublattices are equivalent under statistical averaging. Meanwhile, the system is also driven from a trivial insulator ($\eta = 0$) to a QSH phase ($\eta = 0.5$). Therefore, we can attribute such a topological insulator phase to the bulk topology protected by the average A/B sublattice symmetry which is preserved in the presence of adsorption disorder. Based on the above analysis, we can intuitively conclude that the obtained phase is a newly TAI phase driven by the mechanism of disorder-recovered average symmetry, as illustrated in Fig. 1.

In order to better describe the relationship between disorder-recovered average symmetry mechanism and TAI phase, we adopt a physical quantity $P = \frac{\langle \rho_A \rangle - \langle \rho_B \rangle}{\langle \rho_A \rangle + \langle \rho_B \rangle}$, where $\langle \rho_A \rangle$ is the average LDOS of all the A sites, and so is $\langle \rho_B \rangle$. The blue solid line in Fig. 3(f) shows the evolution of P with η, and P decreases gradually as η increases. When $\eta = 0$, the system belongs to a trivial insulator. P reaches the maximum, suggesting the strongly broken of sublattice symmetry. By increasing η from 0 to 0.5, the system experiences a phase transition

from a trivial phase to a TAI phase. In particular, $P = 0$ for $\eta = 0.5$, that is $\langle \rho_A \rangle = \langle \rho_B \rangle$, and A/B sublattice plays equal roles on average. Nevertheless, by randomly selecting 20 pairs of adjacent A and B sites in the central region, we find local value $P_L = \frac{\rho_A - \rho_B}{\rho_A + \rho_B}$ are not always equal to zero. In Fig. 3(f), the P_L values of these sites are marked by the red stars, and ρ_A is not equal to ρ_B locally. These behaviors imply that although the A/B sublattice symmetry is restored on average, the local sublattice symmetry is still broken when $\eta = 0.5$. Further increasing η, P continues to decrease, the system turns into a trivial insulator. At this time, $\langle \rho_A \rangle < \langle \rho_B \rangle$, suggesting the broken of sublattice symmetry again. Therefore, it is the random adsorption that recovers the A/B sublattice symmetry on average and leads to the TAI phase in graphene. The proposed TAI states are driven by the distribution of disorder with an average symmetry and cannot be described by the self-consistent Born approximation [13,15,28].

In earlier theoretical works, it is reported by the first-principle calculations that for certain noble-metal adatoms (i.e., Cu, Ag, Au) with strong SOC, the top site adsorption in graphene is favored [51,52]. From the experimental aspect, if the random configuration of adsorption for A and B sublattice is achieved and adatom cluster is avoided [53–55], the random adsorption can be fixed by encapsulating graphene by silicon carbide or hexagonal boron nitride. Therefore, this theoretically predicted topological state in graphene may be accessible in experiment. Furthermore, in a conventional TAI, one has to adjust the disorder strength. Alternatively, for the model in this section, one does not have to tune the disorder strength. Thus it also brings advantages for realizing the TAI phase in classic wave systems. For example, in the LC circuit, the adatoms with fixed on-site energy are introduced by grounding capacitors with fixed values. The detailed study will be shown in Sec. V.

IV. TOPOLOGICAL ANDERSON INSULATOR VIA AVERAGE TIME-REVERSAL SYMMETRY

In this section we investigate the topological state of graphene with magnetic adatoms. As described by Eq. (2), the adatoms introduce the planar magnetization with an exchange field strength λ, and the direction $\mathbf{B} = (B_x, B_y, 0)$ can be tuned by an external magnetic field $\mathbf{B}$. The special case of planar magnetization is considered because the z direction of magnetization will not couple the two spin components and will not open an energy gap. Here we concentrate on two cases. One is an ordered sample with uniform magnetization in the central region, for example, taking $\mathbf{B}$ along the x direction, shown in Fig. 4(a). The planar magnetization distinguishes the x direction from other directions, which breaks the time-reversal (TR) symmetry of the system, resembling Fig. 1(a). In such a case, the original gapless helical edge modes are gapped as shown by the energy band structure in Fig. 4(b). Therefore, the sample becomes a trivial insulator.

Another case is a disordered sample with magnetization arbitrarily oriented in the x-y plane, e.g., $\mathbf{B} = (\cos\theta, \sin\theta, 0)$ with θ uniformly distributed in $[0, 2\pi)$, as shown in Fig. 4(c). In experiment, such a case is easy to be realized. Compared with the former case, we remove the magnetic field and raise the temperature above the critical point. Due to thermal dy-
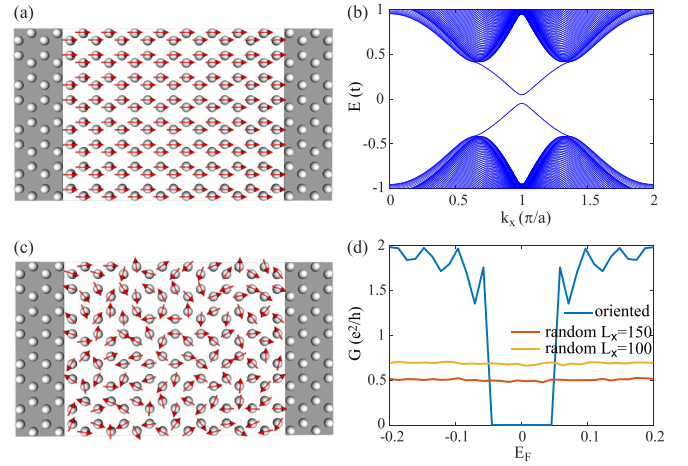

FIG. 4. (a) and (c) Schematic diagrams for the two-terminal devices under oriented and random exchange fields, respectively. (b) The band structure for the central region of device (a). (d) Differential conductance G versus Fermi energy E_F in two such cases. Here we set $t_1 = 1$, $t_2 = 0.08$, $\lambda = 0.05$. The sample size is $N = 50$, $L_x = 150$ for blue and red curves, $L_x = 100$ for the yellow curve.

namics, the magnetization is randomized in all directions. If adatoms have random local magnetization, then no direction has specificity. On average, it seems that there is no net exchange field and no destruction of TR symmetry. Similar to the mechanism in Fig. 1(b), it is doubtful whether it can still restore some topological properties that host without the exchange field.

To confirm such a speculation, we next pay attention to the transport properties of the clean sample (oriented exchange field) and disordered sample (random exchange field), respectively. Figure 4(d) plots the differential conductance G as a function of Fermi energy E_F. For the clean sample (blue solid line), G is zero for energies inside the gap and there is no state here, which is in agreement with the band spectrum of Fig. 4(b). However, for the disordered sample (red solid line), G is nonzero in this energy range, manifesting that there are gapless states inside the band gap [56]. The system may capture a TAI phase.

To get a better insight into the topological properties of the system, we present the LDOS of two such different samples. Similar to the previous case, only the LDOS of the middle layers of the central region are plotted. For the clean sample, the state vanishes in Fig. 5(a), which exhibits its insulating nature. After randomizing the local magnetization and recalculating the LDOS, as shown in Fig. 5(b), several states localized on both boundaries appear. Then the local current distributions $J_x(y)$ are shown in Fig. 5(c). Obviously the local current is zero for a clean sample (gray solid line), manifesting the absence of state. However, for a disordered sample (green solid line), the currents flow along both the upper and lower boundaries. From the calculation results of LDOS and local current distributions, the existence of topological nontrivial edge states is identified and the differential conductance is also caused by the edge states. Furthermore, the red solid line gives the summation of the local currents in the random exchange field. Contrary to the nonmagnetic atom adsorption
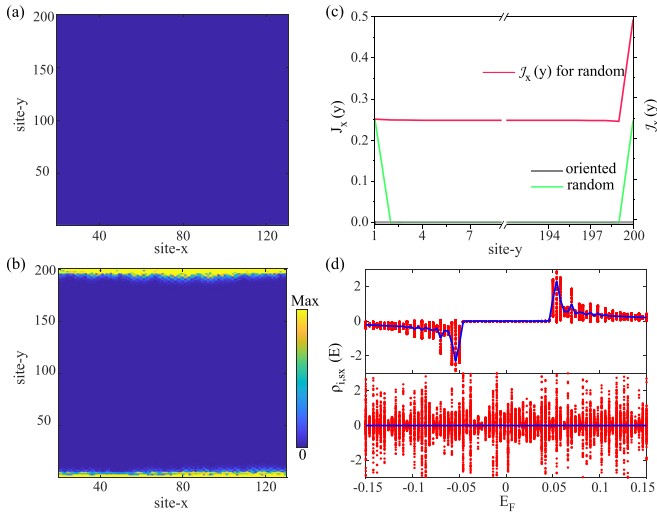
FIG. 5. The left column is the LDOS of the samples under (a) oriented and (b) random exchange fields, respectively. (c) The spatial distributions $J_x(y)$ and the summation of local currents $\mathcal{J}_x(y)$ for two devices. (d) Evolution of ρ_{i,s_x} with Fermi energy E_F. The plots above and below correspond respectively to the samples in Figs. 4(a) and 4(c). The red dots are the ρ_{i,s_x} for each disordered site and the blue solid line is the average. The sample size is $N = 50$, $L_x = 150$. Here the Fermi energy is $E_F = 0$ for (a) to (c), and the other parameters are the same as those in Fig. 4.

case, the summation $\mathcal{J}_x(y)$ is not equal to $2e^2V/h$, indicating that a certain degree of backscattering exists in edge states. Through the above analysis, one can demonstrate that when the direction of planar magnetization becomes disordered, the system will be transformed from a trivial insulator to a TAI phase accompanied by gapless edge states.

In both cases we introduce the exchange field on the lattice, the only difference being the orientation of planar magnetization. When the orientation is fixed, the TR symmetry of the system is destroyed and a band gap appears, which is topologically trivial. However, the random exchange field holds the average TR symmetry, making it possible to exhibit topological phase as demonstrated above. Hence, we can preliminarily attribute that such a topological state is protected by the mechanism of disorder-recovered average TR symmetry, as illustrated in Fig. 1.

To further understand the relationship between average TR symmetry and the TAI phase, we define $S_{i,x}$ as the expectation value of spin operator s_x in the x direction:

$$S_{i,x} = \left\langle (C_{i,\uparrow}^\dagger, C_{i,\downarrow}^\dagger) \begin{pmatrix} 0 & 1 \\ 1 & 0 \end{pmatrix} \begin{pmatrix} C_{i,\uparrow} \\ C_{i,\downarrow} \end{pmatrix} \right\rangle. \tag{5}$$

After utilizing the Keldysh equations [57] and Green's function [58], the expression of the local spin density of states for $S_{i,x}$ at energy E is obtained:

$$\rho_{i,s_x}(E) = \frac{1}{\pi} \text{Im}[G_{\uparrow,\downarrow}^r(i,i;E) + G_{\downarrow,\uparrow}^r(i,i;E)]. \tag{6}$$

For convenience, we only consider the atoms on the top and bottom edges. The red dots in Fig. 5(d) represent ρ_{i,s_x} of each site and the blue solid line is the average. The upper plot

shows ρ_{i,s_x} of the clean sample versus E_F. We notice that, except for an energy window from -0.048 to 0.048, the ρ_{i,s_x} are not equal to zero for both the red dots and blue solid line, suggesting that both global and local TR symmetries are broken. Since ρ_{i,s_x} is zero in the range about $[-0.048, 0.048]$, there is no state, representing a trivial insulator. The lower panel of Fig. 5(d) plots ρ_{i,s_x} for the disordered sample. The present sample has entered into a TAI phase according to previous analysis [see Figs. 4 and 5]. The ρ_{i,s_x} of each site has a positive or negative value, and the overall average value is zero, suggesting that although the TR symmetry is unbroken on average, the TR symmetry is still broken locally. Although the average TR symmetry recovers the helical edge states for the TAI phase, the loss of local TR symmetry can still cause the backscattering between the counterpropagating helical edge states. This result explains why the differential conductance in the disordered sample [see red solid line in Fig. 4(d)] is not quantized.

The above conclusion also reminds us that for several symmetry-protected topological states, the symmetries required for the existence of the corresponding edge states and exotic transport property are quite different. For example, the gapless surface states (hinge states) are protected by the average space group symmetry (average chiral symmetry) in topological crystalline insulators (higher-order topological insulators), while the quantized transport in this system needs to satisfy both the local and global symmetries. Note that the real topological sample is often the case of the former, which may be an important reason why the surface states can be observed but the quantized transport cannot be measured experimentally. In short, in the disordered sample, the gapless helical edge states reappear and this TAI phase is protected by the average TR symmetry.

The realization of this model in condensed matter systems is supported by the first-principles calculation studies. It demonstrates that some $5d$ transitional metal adatoms (e.g., Hf, Ta, Re, or Os) in graphene can form planar magnetization [59]. In another theoretical work, the planar magnetization could be achieved in a modified Kane-Mele model type material Bi_2NF [60]. The adatoms endow magnetic moments to the surrounding carbon atoms, either an oriented magnetization from an external magnetic field or a random one when above the critical temperature. Thus no matter which adsorption site (top, hollow, or bridge) is preferred, little difference is made: compared to the top adsorption site, adsorption in the bridge or hollow sites is even better because the possible on-site energy shift associated with top adsorption is avoided.

V. REALIZATION OF THE TAI IN AN ELECTRIC CIRCUIT

Only through experimental verification can the theoretical proposal be more complete and convincing. Up to now, the TAI has been experimentally confirmed in only several classical wave systems [28–30]. The reason may be that the control of disorder strength is difficult to achieve in condensed matter systems and is not easy to implement in classical wave systems. Since it is much easier to control the adatom spatial positions, our theoretical proposal can provide an easier solution from the experimental perspective. Simulating
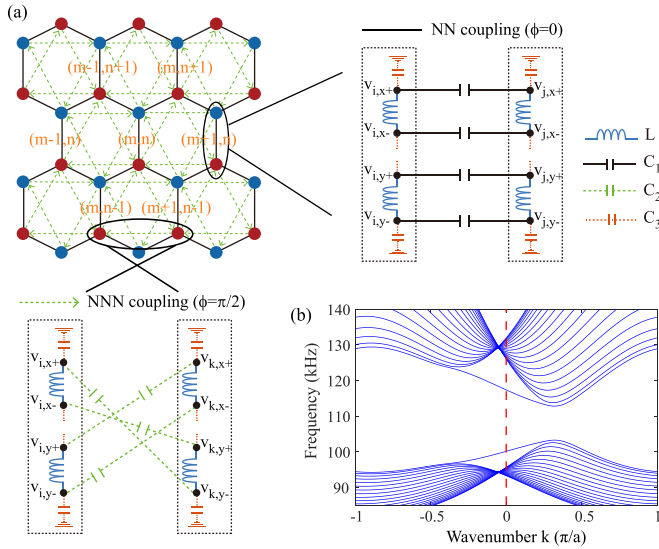
FIG. 6. Setup of the electric circuit. (a) Top-left chart is the schematic diagram of the Kane-Mele model. The black solid (green dashed) lines represent NN (NNN) hoppings. Each lattice site is composed of a pair of inductors with inductance L. The schematic diagrams for the construction of NN and NNN hoppings in an electric circuit are shown in the top-right and bottom-left charts, respectively. The capacitor with capacitance C_3 is the grounding capacitor. (b) Band structure of the circuit lattice when $\eta = 1$, for a strip that is infinite along x and 20 unit cells width along y direction. The circuit parameters are $L = 3.3$ mH, $C_1 = 330$ pF, $C_2 = 19.8$ pF, and $C_3 = 429$ pF.

topological states with circuits has gained great attention in recent years [21,23,61–78] due to its ease of fabrication and measurement compared with other classical platforms. The first model in Sec. III can be implemented by a LC circuit in which the role of the nonmagnetic adatom is played by capacitors. The randomization of adatoms position, i.e., the disorder we proposed, in a circuit can be simulated by adjusting the position of the grounding capacitors. Alternatively, in the second model in Sec. IV, since the magnetic moment breaks the time-reversal symmetry, the corresponding LC circuit should also bear such a characteristic. In a recent work the operational amplifiers are used in the LC circuit system to break the time-reversal symmetry [79].

In the following we present a feasible scheme to realize the TAI phase in the nonmagnetic adatom adsorption model by utilizing a LC circuit system. The schematic diagram of the Kane-Mele model with NN (black solid lines) and NNN (green dashed lines) hoppings is shown in the top-left chart of Fig. 6(a). The NNN hoppings have $\pi/2$ phase shifts (spin-up component) in the direction indicated by the arrows and the NN hoppings experience zero phase shift. The key to mapping the model into the circuit network is how to construct such two hoppings and introduce the on-site energy. As shown in the black dashed rectangular box of Fig. 6(a), each lattice site is composed of two inductors X and Y with inductance L, and the inductor contains two nodes (black dots). The voltages of these four nodes are marked by $V_{i,X+}, V_{i,X-}, V_{i,Y+}, V_{i,Y-}$. The voltages across the inductors are $U_X = V_{i,X+} - V_{i,X-}$, $U_Y = V_{i,Y+} - V_{i,Y-}$, respectively. The top-right chart shows

the realization of NN hopping, four capacitors with capacitance C_1 are used to directly link the two sties labeled by i and j, with $V_{i,\alpha}$ connecting to $V_{j,\alpha}$ ($\alpha = X+, X-, Y+, Y-$). To simulate the NNN hopping, $[V_{i,X+}, V_{i,X-}, V_{i,Y+}, V_{i,Y-}]$ is cross connected to $[V_{k,Y-}, V_{k,Y+}, V_{k,X+}, V_{k,X-}]$ via capacitors with capacitance C_2, as presented in the bottom-left chart. The on-site energy can be introduced by connecting four grounding capacitors with capacitance C_3 to the nodes of the lattice site.

To present the validity of the designed circuit, according to Kirchhoff's laws, we write the circuit equations when $\eta = 1$. Defining $U_{\uparrow,\downarrow} = U_X \pm iU_Y$, the eigenequations of spin-up and spin-down states are obtained (the detailed derivation can be found in Appendix A), and they are related by the TR symmetry [62–65]

$$E\begin{pmatrix} U_{\mathbf{k},\uparrow}^A \\ U_{\mathbf{k},\uparrow}^B \end{pmatrix} = \begin{pmatrix} P_{\mathbf{k}}(\phi) - U & T_{\mathbf{k}} \\ T_{\mathbf{k}}^* & P_{\mathbf{k}}(-\phi) \end{pmatrix} \begin{pmatrix} U_{\mathbf{k},\uparrow}^A \\ U_{\mathbf{k},\uparrow}^B \end{pmatrix},$$

$$E\begin{pmatrix} U_{\mathbf{k},\downarrow}^A \\ U_{\mathbf{k},\downarrow}^B \end{pmatrix} = \begin{pmatrix} P_{\mathbf{k}}(-\phi) - U & T_k \\ T_{\mathbf{k}}^* & P_{\mathbf{k}}(\phi) \end{pmatrix} \begin{pmatrix} U_{\mathbf{k},\downarrow}^A \\ U_{\mathbf{k},\downarrow}^B \end{pmatrix}, \quad (7)$$

where $E = 3t_1 + 6t_2 - 2\omega_0^2/\omega^2$, $\omega_0 = 1/\sqrt{LC}$. C is a reference capacitance such that $C_1 = t_1 C, C_2 = t_2 C, C_3 = UC$. The elements in Eq. (7) are $T_{\mathbf{k}} = t_1(e^{i\mathbf{k}\cdot\mathbf{e}_1} + e^{i\mathbf{k}\cdot\mathbf{e}_2} + e^{i\mathbf{k}\cdot\mathbf{e}_3})$, $P_{\mathbf{k}} = 2t_2[\cos(\mathbf{k}\cdot\mathbf{v}_1 + \phi) + \cos(\mathbf{k}\cdot\mathbf{v}_2 + \phi) + \cos(\mathbf{k}\cdot\mathbf{v}_3 + \phi)]$, and $\phi = \pi/2$. $\mathbf{e}_i(i = 1, 2, 3)$ and $\mathbf{v}_j(j = 1, 2, 3)$ are NN and NNN bond vectors, respectively. The right side of Eq. (7) is indeed the Hamiltonian of the modified Kane-Mele model with $-U$ representing the on-site energy on sublattice A. Equations (7) and (1) share the same noninteracting Hamiltonian and nearly all physical quantities defined based on the Hamiltonian should be the same. Supposing the above Hamiltonian has eigenvalues $E = \epsilon(k)$, the frequency f_k and energy $\epsilon(k)$ satisfy $f_k = \frac{\omega}{2\pi} = \frac{1}{2\pi}\frac{1}{\sqrt{LC}}\sqrt{\frac{2}{3t_1+6t_2-\epsilon(k)}}$. Therefore, it is straightforward to infer that our designed circuit can implement the topological state. For the sake of convenience, we only focus on the spin-up component. One obtains $t_1 = 1$, $t_2 = 0.06$, $U = 1.3$ (the same model parameters in Sec. III) by choosing appropriate circuit parameters to be $C = 330$ pF, $C_1 = 330$ pF, $C_2 = 19.8$ pF, and $C_3 = 429$ pF. Figure 6(b) shows the calculated one-dimensional band spectrum of the circuit lattice when $\eta = 1$, with the vertical axis being frequency f_k. It is in agreement with Fig. 2(b), the system is a trivial insulator with a frequency gap. Now we turn to a finite circuit structure with 4×8 sites to clarify the realization of the TAI via average sublattice symmetry in a LC circuit by performing steady state simulation. We randomize the grounding C_3 positions on the honeycomb lattice to simulate the randomization of the adatoms position, which tunes η. In this paper we use *LTspice* software to perform all circuit simulations [80]. To obtain the mode response of the circuit, we excite the upper-leftmost corner site (marked by a red star) by placing the sources where $S_X = \cos(\omega t)$ and $S_Y = \sin(\omega t)$ on the X and Y inductors, respectively. Voltages with $90°$ relative phase shift is to solely excite the spin-up state [65]. The voltage amplitudes on the Y inductors at different sites are measured. Figures 7(a) and 7(b) display the measured voltage amplitude distributions for the clean sample ($\eta = 1$) and disordered sample ($\eta = 0.5$) at 109 kHz, respectively. When
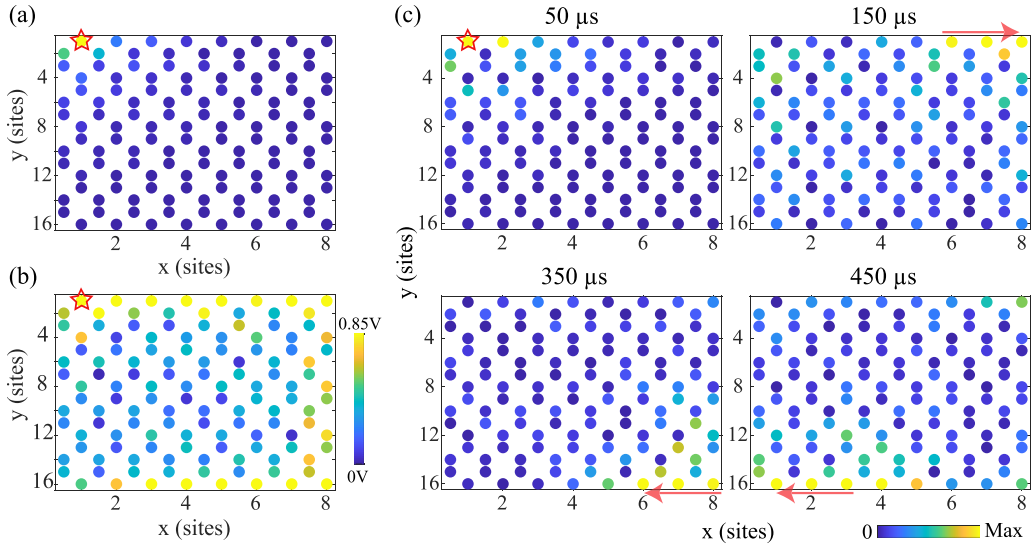
FIG. 7. Propagation characteristic of the edge state in a finite lattice. (a) and (b) The steady state voltage amplitude distributions at 109 kHz when $\eta = 1$ and $\eta = 0.5$, respectively. Voltage sources with $90°$ phase difference are placed on the inductors X and Y at the upper-leftmost corner site (marked by a red star) so as to excite the spin-up edge state. (c) Time-domain circuit simulations for $\eta = 0.5$, in which a time-dependent Gaussian input signal excites an edge state that propagates rightward along the upper edge. Voltage amplitude distributions at different times show the propagation of an edge state. The directions of propagation are represented by red arrows. All other parameters are the same as those in Fig. 6.

$\eta = 1$, the voltage amplitudes are vanishingly small except for a few lattice sites near the driving source. In contrast, when $\eta = 0.5$, it is apparent that dominant voltage signals exist at both edge sites and no bulk penetration, manifesting the realization of the edge state. This result agrees well with theoretical prediction.

To further characterize the edge state, we perform time-domain simulations of the designed open circuit. Using a Gaussian input signal with time delay $t_0 = 50$ μs, width $dt = 50$ μs, and frequency $f = 109$ kHz, in which voltages $S_X = e^{-\frac{(t-t_0)^2}{dt^2}}\cos(\omega t)$ and $S_Y = e^{-\frac{(t-t_0)^2}{dt^2}}\sin(\omega t)$ are placed on the X and Y inductors at the upper-leftmost corner site, respectively, in order to generate a spin-up source $S_\uparrow = e^{-\frac{(t-t_0)^2}{dt^2}}e^{i\omega t}$ [64]. Figure 7(c) shows the voltage amplitude distributions at different times when $\eta = 0.5$. In this configuration, the driving source will excite the edge state that moves rightward along the upper boundary. At about 150 μs, it reaches the right boundary. At around 350 μs, the edge state at the bottom boundary is excited and continues to move leftward. We also perform a time-domain simulation for the clean sample, as expected, the state cannot be transmitted. More details are given in Appendix B. In a word, through circuit simulation and voltage measurement, the disorder-induced edge state is identified, suggesting the emergence of the TAI phase which is protected by disorder recovery of an average A/B sublattice symmetry.

VI. SUMMARY

In this paper we propose the realization of TAIs via average symmetries and reveal their nontrivial topological properties in a modified Kane-Mele model with two types of adatoms. For the nonmagnetic adatom case, randomly spatial distributed adatoms recover an average A/B sublattice and lead to the TAI phase. For the magnetic adatom case, the average TR symmetry-protected TAI is caused by the randomization in the direction of local planar magnetization.

We also provide a scheme to realize the proposed TAI phase in LC circuits. Through direct circuit simulation, the experimental feasibility for such a topological state is verified. Our work depends on the understanding of the relationship between the TAI and symmetries under statistical averaging, and broadens the way toward using circuit materials for future studies of topological states.
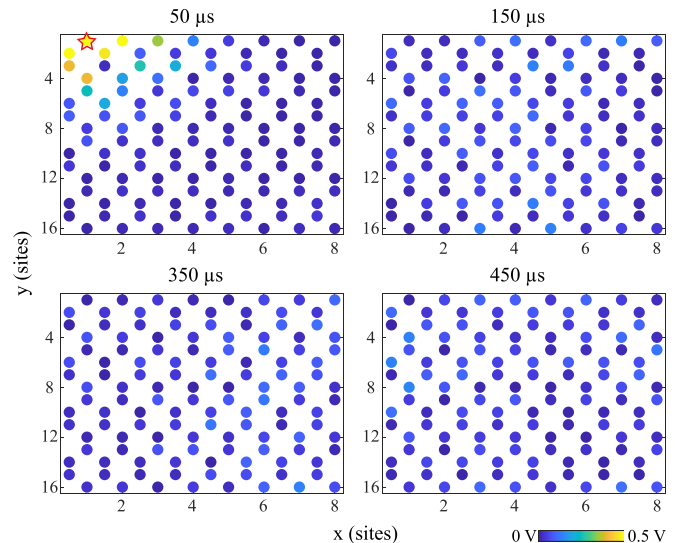

FIG. 8. Voltage amplitude distributions at different times. The construction of the circuit and the location of sources are the same as those in Fig. 7(c) of the main text except for $\eta = 1$.

APPENDIX A: DERIVATION OF AN ELECTRIC CIRCUIT MODEL

We turn to the correspondence between the nonmagnetic atom adsorption model and the designed circuit network. In our model, each lattice site contains a pair of inductors with four nodes. Each site is connected to others through three NN and six NNN hoppings, as shown in Fig. 6(a) of the main text. Additionally, all A sites are grounded by C_3 when $\eta = 1$. Based on Kirchhoff's laws, the circuit equation of node X^+/X^- of inductor X at site (m, n, A) can be written as

$$
\begin{aligned}
&\left(V_{m,n,X^+}^A - V_{m,n,X^-}^A\right)/i\omega L + i\omega t_1 C\left[\left(V_{m,n,X^+}^A - V_{m,n,X^+}^B\right) + \left(V_{m,n,X^+}^A - V_{m+1,n-1,X^+}^B\right) + \left(V_{m,n,X^+}^A - V_{m,n-1,X^+}^B\right)\right] \\
&\quad + i\omega t_2 C\left[\left(V_{m,n,X^+}^A - V_{m+1,n,Y^+}^A\right) + \left(V_{m,n,X^+}^A - V_{m,n+1,Y^-}^A\right) + \left(V_{m,n,X^+}^A - V_{m-1,n+1,Y^+}^A\right) + \left(V_{m,n,X^+}^A - V_{m-1,n,Y^-}^A\right)\right. \\
&\quad \left. + \left(V_{m,n,X^+}^A - V_{m,n-1,Y^+}^A\right) + \left(V_{m,n,X^+}^A - V_{m+1,n-1,Y^-}^A\right)\right] + i\omega U C V_{m,n,X^+}^A = 0,
\end{aligned}
\tag{A1}
$$

$$
\begin{aligned}
&\left(V_{m,n,X^-}^A - V_{m,n,X^+}^A\right)/i\omega L + i\omega t_1 C\left[\left(V_{m,n,X^-}^A - V_{m,n,X^-}^B\right) + \left(V_{m,n,X^-}^A - V_{m+1,n-1,X^-}^B\right) + \left(V_{m,n,X^-}^A - V_{m,n-1,X^-}^B\right)\right] \\
&\quad + i\omega t_2 C\left[\left(V_{m,n,X^-}^A - V_{m+1,n,Y^-}^A\right) + \left(V_{m,n,X^-}^A - V_{m,n+1,Y^+}^A\right) + \left(V_{m,n,X^-}^A - V_{m-1,n+1,Y^-}^A\right) + \left(V_{m,n,X^-}^A - V_{m-1,n,Y^+}^A\right)\right. \\
&\quad \left. + \left(V_{m,n,X^-}^A - V_{m,n-1,Y^-}^A\right) + \left(V_{m,n,X^-}^A - V_{m+1,n-1,Y^+}^A\right)\right] + i\omega U C V_{m,n,X^-}^A = 0.
\end{aligned}
\tag{A2}
$$

The difference between Eqs. (A1) and (A2) yields

$$
\begin{aligned}
U_{m,n,X}^A = -\frac{\omega^2}{2\omega_0^2}\Big[&-(3t_1 + 6t_2 + U)U_{m,n,X}^A + t_1\left(U_{m,n,X}^B + U_{m+1,n-1,X}^B + U_{m,n-1,X}^B\right) \\
&+ t_2\left(-U_{m,n+1,Y}^A + U_{m,n-1,Y}^A + U_{m+1,n,Y}^A - U_{m-1,n,Y}^A + U_{m-1,n+1,Y}^A - U_{m+1,n-1,Y}^A\right)\Big],
\end{aligned}
\tag{A3}
$$

where $\omega_0 = \frac{1}{\sqrt{LC}}$. C acts as a reference capacitance so $C_1 = t_1 C$, $C_2 = t_2 C$, $C_3 = UC$. We can also derive the equations for inductor Y at site A, as well as for site B following the same route:

$$
\begin{aligned}
U_{m,n,Y}^A = -\frac{\omega^2}{2\omega_0^2}\Big[&-(3t_1 + 6t_2 + U)U_{m,n,Y}^A + t_1\left(U_{m,n,Y}^B + U_{m+1,n-1,Y}^B + U_{m,n-1,Y}^B\right) \\
&+ t_2\left(U_{m,n+1,X}^A - U_{m,n-1,X}^A - U_{m+1,n,X}^A + U_{m-1,n,X}^A - U_{m-1,n+1,X}^A + U_{m+1,n-1,X}^A\right)\Big],
\end{aligned}
\tag{A4}
$$

$$
\begin{aligned}
U_{m,n,X}^B = -\frac{\omega^2}{2\omega_0^2}\Big[&-(3t_1 + 6t_2)U_{m,n,X}^B + t_1\left(U_{m,n,X}^A + U_{m,n+1,X}^A + U_{m-1,n+1,X}^A\right) \\
&+ t_2\left(U_{m,n+1,Y}^B - U_{m,n-1,Y}^B - U_{m+1,n,Y}^B + U_{m-1,n,Y}^B - U_{m-1,n+1,Y}^B + U_{m+1,n-1,Y}^B\right)\Big],
\end{aligned}
\tag{A5}
$$

$$
\begin{aligned}
U_{m,n,Y}^B = -\frac{\omega^2}{2\omega_0^2}\Big[&-(3t_1 + 6t_2)U_{m,n,Y}^B + t_1\left(U_{m,n,Y}^A + U_{m,n+1,Y}^A + U_{m-1,n+1,Y}^A\right) \\
&+ t_2\left(-U_{m,n+1,X}^B + U_{m,n-1,X}^B + U_{m+1,n,X}^B - U_{m-1,n,X}^B + U_{m-1,n+1,X}^B - U_{m+1,n-1,X}^B\right)\Big].
\end{aligned}
\tag{A6}
$$

Defining $U_{\uparrow,\downarrow} = U_X \pm iU_Y$, the above equations reduce to

$$
\begin{aligned}
\left(3t_1 + 6t_2 - 2\frac{\omega_0^2}{\omega^2}\right)U_{m,n,\uparrow}^A = &-UU_{m,n,\uparrow}^A + t_1\left(U_{m,n,\uparrow}^B + U_{m+1,n-1,\uparrow}^B + U_{m,n-1,\uparrow}^B\right) \\
&+ t_2\left(e^{i\phi}U_{m,n+1,\uparrow}^A + e^{-i\phi}U_{m,n-1,\uparrow}^A + e^{-i\phi}U_{m+1,n,\uparrow}^A + e^{i\phi}U_{m-1,n,\uparrow}^A + e^{-i\phi}U_{m-1,n+1,\uparrow}^A + e^{i\phi}U_{m+1,n-1,\uparrow}^A\right),
\end{aligned}
\tag{A7}
$$

$$
\begin{aligned}
\left(3t_1 + 6t_2 - 2\frac{\omega_0^2}{\omega^2}\right)U_{m,n,\uparrow}^B = &\; t_1\left(U_{m,n,\uparrow}^A + U_{m,n+1,\uparrow}^A + U_{m-1,n+1,\uparrow}^A\right) \\
&+ t_2\left(e^{-i\phi}U_{m,n+1,\uparrow}^B + e^{i\phi}U_{m,n-1,\uparrow}^B + e^{i\phi}U_{m+1,n,\uparrow}^B + e^{-i\phi}U_{m-1,n,\uparrow}^B + e^{i\phi}U_{m-1,n+1,\uparrow}^B + e^{-i\phi}U_{m+1,n-1,\uparrow}^B\right),
\end{aligned}
\tag{A8}
$$

where $\phi = \frac{\pi}{2}$. For simplicity, the $U_{i,\downarrow}$ component of the model is not shown here.

By applying a spatial Fourier transform, we obtain the eigenequations for spin-up and spin-down states

$$E \begin{pmatrix} U^A_{\mathbf{k},\uparrow} \\ U^B_{\mathbf{k},\uparrow} \end{pmatrix} = \begin{pmatrix} P_{\mathbf{k}}(\phi) - U & T_{\mathbf{k}} \\ T^*_{\mathbf{k}} & P_{\mathbf{k}}(-\phi) \end{pmatrix} \begin{pmatrix} U^A_{\mathbf{k},\uparrow} \\ U^B_{\mathbf{k},\uparrow} \end{pmatrix},$$

$$E \begin{pmatrix} U^A_{\mathbf{k},\downarrow} \\ U^B_{\mathbf{k},\downarrow} \end{pmatrix} = \begin{pmatrix} P_{\mathbf{k}}(-\phi) - U & T_k \\ T^*_{\mathbf{k}} & P_{\mathbf{k}}(\phi) \end{pmatrix} \begin{pmatrix} U^A_{\mathbf{k},\downarrow} \\ U^B_{\mathbf{k},\downarrow} \end{pmatrix}, \quad \text{(A9)}$$

where $E = 3t_1 + 6t_2 - 2\omega_0^2/\omega^2$, $T_{\mathbf{k}} = t_1(e^{i\mathbf{k}\cdot\mathbf{e}_1} + e^{i\mathbf{k}\cdot\mathbf{e}_2} + e^{i\mathbf{k}\cdot\mathbf{e}_3})$, $P_{\mathbf{k}} = 2t_2[\cos(\mathbf{k}\cdot\mathbf{v}_1 + \phi) + \cos(\mathbf{k}\cdot\mathbf{v}_2 + \phi) + \cos(\mathbf{k}\cdot$

$\mathbf{v}_3 + \phi)]$. Consequently, it is straightforward to infer that our designed electric circuit can be used to characterize the topological properties of the nonmagnetic atom adsorption model.

APPENDIX B: TIME-DOMAIN CIRCUIT SIMULATION

Figure 8 shows the time-domain simulations when $\eta = 1$. One can see that a spin-up state is excited at the upper-leftmost corner site. However, due to the broken of A/B sublattice symmetry, it is obvious that the state cannot be transmitted.

[1] P. W. Anderson, Absence of diffusion in certain random lattices, Phys. Rev. **109**, 1492 (1958).

[2] E. Abrahams, P. W. Anderson, D. C. Licciardello, and T. V. Ramakrishnan, Scaling Theory of Localization: Absence of Quantum Diffusion in Two Dimensions, Phys. Rev. Lett. **42**, 673 (1979).

[3] P. A. Lee and A. D. Stone, Universal Conductance Fluctuations in Metals, Phys. Rev. Lett. **55**, 1622 (1985).

[4] K. Nomura and N. Nagaosa, Surface-Quantized Anomalous Hall Current and the Magnetoelectric Effect in Magnetically Disordered Topological Insulators, Phys. Rev. Lett. **106**, 166802 (2011).

[5] L. Sheng, D. N. Sheng, C. S. Ting, and F. D. M. Haldane, Nondissipative Spin Hall Effect via Quantized Edge Transport, Phys. Rev. Lett. **95**, 136602 (2005).

[6] W. Ren, Z. H. Qiao, J. Wang, Q. F. Sun, and H. Guo, Universal Spin-Hall Conductance Fluctuations in Two Dimensi, Phys. Rev. Lett. **97**, 066603 (2006).

[7] F. Evers and A. D. Mirlin, Anderson transitions, Rev. Mod. Phys. **80**, 1355 (2008).

[8] H. L. Li, C. Z. Chen, H. Jiang, and X. C. Xie, Coexistence of Quantum Hall and Quantum Anomalous Hall Phases in Disordered MnBi$_2$Te$_4$, Phys. Rev. Lett. **127**, 236402 (2021).

[9] P. Titum, N. H. Lindner, M. C. Rechtsman, and G. Refael, Disorder-Induced Floquet Topological Insulators, Phys. Rev. Lett. **114**, 056801 (2015).

[10] S. G. Cheng, R. Z. Zhang, J. J. Zhou, H. Jiang, and Q. F. Sun, Perfect valley filter based on a topological phase in a disordered Sb monolayer heterostructure, Phys. Rev. B **97**, 085420 (2018).

[11] C. Z. Chen, J. T. Song, H. Jiang, Q. F. Sun, Z. Q. Wang, and X. C. Xie, Disorder and Metal-Insulator Transitions in Weyl Semimetals, Phys. Rev. Lett. **115**, 246603 (2015).

[12] E. Prodan, T. L. Hughes, and B. A. Bernevig, Entanglement Spectrum of a Disordered Topological Chern Insulator, Phys. Rev. Lett. **105**, 115501 (2010).

[13] J. Li, R. L. Chu, J. K. Jain, and S. Q. Shen, Topological Anderson Insulator, Phys. Rev. Lett. **102**, 136806 (2009).

[14] H. Jiang, L. Wang, Q. F. Sun, and X. C. Xie, Numerical study of the topological Anderson insulator in HgTe/CdTe quantum wells, Phys. Rev. B **80**, 165316 (2009).

[15] C. W. Groth, M. Wimmer, A. R. Akhmerov, J. Tworzydlo, and C. W. J. Beenakker, Theory of the Topological Anderson Insulator, Phys. Rev. Lett. **103**, 196805 (2009).

[16] H. M. Guo, G. Rosenberg, G. Refael, and M. Franz, Topological Anderson Insulator in Three Dimensions, Phys. Rev. Lett. **105**, 216601 (2010).

[17] J. T. Song, H. W. Liu, H. Jiang, Q. F. Sun, and X. C. Xie, Dependence of topological Anderson insulator on the type of disorder, Phys. Rev. B **85**, 195125 (2012).

[18] Y. Su, Y. Avishai, and X. R. Wang, Topological Anderson insulators in systems without time-reversal symmetry, Phys. Rev. B **93**, 214206 (2016).

[19] B. A. Bernevig, T. L. Hughes, and S. C. Zhang, Quantum spin Hall effect and topological phase transition in HgTe quantum wells, Science **314**, 1757 (2006).

[20] M. König, S. Wiedmann, C. Brüne, A. Roth, H. Buhmann, L. W. Molenkamp, X. L. Qi, and S. C. Zhang, Quantum spin Hall insulator state in HgTe quantum wells, Science **318**, 766 (2007).

[21] Z. Q. Zhang, B. L. Wu, J. T. Song, and Hua Jiang, Topological Anderson insulator in electric circuits, Phys. Rev. B **100**, 184202 (2019).

[22] Y. B. Yang, K. Li, L. M. Duan, and Y. Xu, Higher-order topological Anderson insulators, Phys. Rev. B **103**, 085408 (2021).

[23] W. X. Zhang, D. Y. Zou, Q. S. Pei, W. J. He, J. C. Bao, H. J. Sun, and X. D. Zhang, Experimental Observation of Higher-Order Topological Anderson Insulators, Phys. Rev. Lett. **126**, 146802 (2021).

[24] C. A. Li, B. Fu, Z. A. Hu, J. Li, and S. Q. Shen, Topological Phase Transitions in Disordered Electric Quadrupole Insulators, Phys. Rev. Lett. **125**, 166801 (2020).

[25] H.-C. Hsu and T.-W. Chen, Topological Anderson insulating phases in the long-range Su-Schrieffer-Heeger model, Phys. Rev. B **102**, 205425 (2020).

[26] A. Altland, D. Bagrets, L. Fritz, A. Kamenev, and H. Schmiedt, Quantum Criticality of Quasi-One-Dimensional Topological Anderson Insulators, Phys. Rev. Lett. **112**, 206602 (2014).

[27] A. Altland, D. Bagrets, and A. Kamenev, Topology versus Anderson localization: Nonperturbative solutions in one dimension, Phys. Rev. B **91**, 085429 (2015).

[28] E. J. Meier, F. A. An, A. Dauphin, M. Maffei, P. Massignan, T. L. Hughes, and B. Gadway, Observation of the topological Anderson insulator in disordered atomic wires, Science **362**, 929 (2018).

[29] S. Stützer, Y. Plotnik, Y. Lumer, P. Titum, N. H. Lindner, M. Segev, M. C. Rechtsman, and A. Szameit, Photonic topological Anderson insulators, Nature (London) **560**, 461 (2018).

[30] G. G. Liu, Y. Yang, X. Ren, H. Xue, X. Lin, Y. H. Hu, H. X. Sun, B. Peng, P. Zhou, Y. Chong, and B. Zhang, Topological Anderson Insulator in Disordered Photonic Crystals, Phys. Rev. Lett. **125**, 133603 (2020).

[31] R. Chen, D. H. Xu, and B. Zhou, Topological Anderson insu-

lator phase in a quasicrystal lattice, Phys. Rev. B **100**, 115311 (2019).

[32] T. Peng, C. B. Hua, R. Chen, D. H. Xu, and B. Zhou, Topological Anderson insulators in an Ammann-Beenker quasicrystal and a snub-square crystal, Phys. Rev. B **103**, 085307 (2021).

[33] H. F. Liu, Z. X. Su, Z. Q. Zhang, and H. Jiang, Topological Anderson insulator in two-dimensional non-Hermitian systems, Chin. Phys. B **29**, 050502 (2020).

[34] H. F. Liu, J. K. Zhou, B. L. Wu, Z. Q. Zhang, and H. Jiang, Real-space topological invariant and higher-order topological Anderson insulator in two-dimensional non-Hermitian systems, Phys. Rev. B **103**, 224203 (2021).

[35] T. Peng, C. B. Hua, R. Chen, Z. R. Liu, D. H. Xu, and B. Zhou, Higher-order topological Anderson insulators in quasicrystals, Phys. Rev. B **104**, 245302 (2021).

[36] C. Wang and X. R. Wang, Disorder-induced quantum phase transitions in three-dimensional second-order topological insulators, Phys. Rev. Res. **2**, 033521 (2020).

[37] X. H. Cui, R. Y. Zhang, Z. Q. Zhang, C. T. Chan, Photonic Z_2 topological Anderson insulators, Phys. Rev. Lett. **129**, 043902 (2022).

[38] Q. Lin, T. Li, L. Xiao, K. Wang, W. Yi, and P. Xue, Observation of non-Hermitian topological Anderson insulator in quantum dynamics, Nat. Commun. **13**, 3229 (2022).

[39] D. W. Zhang, L. Z. Tang, L. J. Lang, H. Yan, and S. L. Zhu, Non-Hermitian topological Anderson insulators, Sci. China: Phys., Mech. Astron. **63**, 267062 (2020).

[40] C. Wang, T. Cheng, Z. R. Liu, F. Liu, and H. Q. Huang, Structural Amorphization-Induced Topological Order, Phys. Rev. Lett. **128**, 056401 (2022).

[41] Y. Xing, L. Zhang, and J. Wang, Topological Anderson insulator phenomena, Phys. Rev. B **84**, 035110 (2011).

[42] L. Fu and C. L. Kane, Topology, Delocalization via Average Symmetry and the Symplectic Anderson Transition, Phys. Rev. Lett. **109**, 246605 (2012).

[43] C. L. Kane and E. J. Mele, Quantum Spin Hall Effect in Graphene, Phys. Rev. Lett. **95**, 226801 (2005).

[44] C. Weeks, J. Hu, J. Alicea, M. Franz, and R. Wu, Engineering a Robust Quantum Spin Hall State in Graphene via Adatom Deposition, Phys. Rev. X **1**, 021001 (2011).

[45] O. Shevtsov, P. Carmier, C. Groth, and X. Waintal, Tunable thermopower in a graphene-based topological insulator, Phys. Rev. B **85**, 245441 (2012).

[46] H. Jiang, Z. H. Qiao, H. W. Liu, J. R. Shi, and Q. Niu, Stabilizing Topological Phases in Graphene via Random Adsorption, Phys. Rev. Lett. **109**, 116803 (2012).

[47] S. Datta, *Electronic Transport in Mesoscopic Systems* (Cambridge University Press, Cambridge, 1995).

[48] W. Long, Q. F. Sun, and J. Wang, Disorder-Induced Enhancement of Transport through Graphene *p-n* Junctions, Phys. Rev. Lett. **101**, 166806 (2008).

[49] F. Xu and J. Wang, Statistical properties of electrochemical capacitance in disordered mesoscopic capacitors, Phys. Rev. B **89**, 245430 (2014).

[50] Y. Y. Zhang, J. P. Hu, B. A. Bernevig, X. R. Wang, X. C. Xie, and W. M. Liu, Quantum blockade and loop currents in graphene with topological defects, Phys. Rev. B **78**, 155413 (2008).

[51] K. Chan, J. B. Neaton, and M. Cohen, First-principles study of metal adatom adsorption on graphene, Phys. Rev. B **77**, 235430 (2008).

[52] J. Ding, Z. H. Qiao, W. X. Feng, Y. G. Yao, and Q. Niu, Engineering quantum anomalous/valley Hall states in graphene via metal-atom adsorption: An *ab-initio* study, Phys. Rev. B **84**, 195444 (2011).

[53] Y. Zhang, N. W. Franklin, R. J. Chen, H. J. Dai, Metal coating on suspended carbon nanotubes and its implication to metal–tube interaction, Chem. Phys. Lett. **331**, 35 (2000).

[54] K. M. McCreary, K. Pi, A. G. Swartz, W. Han, W. Bao, C. N. Lau, F. Guinea, M. I. Katsnelson, and R. K. Kawakami, Effect of cluster formation on graphene mobility, Phys. Rev. B **81**, 115453 (2010).

[55] X. J. Liu, M. Hupalo, C. Z. Wang, W. C. Lu, P. A. Thiel, K. M. Ho, and M. C. Tringides, Growth morphology and thermal stability of metal islands on graphene, Phys. Rev. B **86**, 081414(R) (2012).

[56] We have also calculated the differential conductance *G* and local density of states for a disordered sample with arbitrary magnetization orientation. Similar results are obtained which means there are gapless states inside the band gap. The disordered magnetization with arbitrary orientation contributes a weaker effective planar component, and the differential conductance *G* obtained is larger compared to Fig. 4(d).

[57] A. P. Jauho, N. S. Wingreen, and Y. Meir, Time-dependent transport in interacting and noninteracting resonant-tunneling systems, Phys. Rev. B **50**, 5528 (1994).

[58] B. K. Nikolić, L. P. Zărbo, and S. Souma, Imaging mesoscopic spin Hall flow: Spatial distribution of local spin currents and spin densities in and out of multiterminal spin-orbit coupled semiconductor nanostructures, Phys. Rev. B **73**, 075303 (2006).

[59] H. Zhang, C. Lazo, S. Blügel, S. Heinze, and Y. Mokrousov, Electrically Tunable Quantum Anomalous Hall Effect in Graphene Decorated by 5*d* Transition-Metal Adatoms, Phys. Rev. Lett. **108**, 056802 (2012).

[60] J. J. Zhou, T. Zhou, S. G. Cheng, H. Jiang, and Z. Q. Yang, Engineering a topological quantum dot device through planar magnetization in bismuthene, Phys. Rev. B **99**, 195422 (2019).

[61] E. Zhao, Topological circuits of inductors and capacitors, Ann. Phys. **399**, 289 (2018).

[62] N. Y. Jia, C. Owens, A. Sommer, D. Schuster, and J. Simon, Time- and Site-Resolved Dynamics in a Topological Circuit, Phys. Rev. X **5**, 021031 (2015).

[63] V. V. Albert, L. I. Glazman, and L. Jiang, Topological Properties of Linear Circuit Lattices, Phys. Rev. Lett. **114**, 173902 (2015).

[64] W. W. Zhu, S. S. Hou, Y. Long, H. Chen, and J. Ren, Simulating quantum spin Hall effect in the topological Lieb lattice of a linear circuit network, Phys. Rev. B **97**, 075310 (2018).

[65] W. W. Zhu, Y. Long, H. Chen, and J. Ren, Quantum valley Hall effects and spin-valley locking in topological Kane-Mele circuit networks, Phys. Rev. B **99**, 115410 (2019).

[66] J. Dong, V. Juričić, and B. Roy, Topolectric circuits: Theory and construction, Phys. Rev. Res. **3**, 023056 (2021).

[67] R. Yu, Y. X. Zhao, and A. P. Schnyder, 4D spinless topological insulator in a periodic electric circuit, Nat. Sci. Rev. **7**, 1288 (2020).

[68] T. Hofmann, T. Helbig, C. H. Lee, M. Greiter, and R. Thomale, Chiral Voltage Propagation and Calibration in a Topolectrical Chern Circuit, Phys. Rev. Lett. **122**, 247702 (2019).

[69] M. Ezawa, Electric circuits for non-Hermitian Chern insulators, Phys. Rev. B **100**, 081401(R) (2019).

[70] C. H. Lee, S. Imhof, C. Berger, F. Bayer, J. Brehm, L. W. Molenkamp, T. Kiessling, and R. Thomale, Topolectrical Circuits, Commun. Phys. **1**, 39 (2018).

[71] T. Helbig, T. Hofmann, C. H. Lee, R. Thomale, S. Imhof, L. W. Molenkamp, and T. Kiessling, Band structure engineering and reconstruction in electric circuit networks, Phys. Rev. B **99**, 161114(R) (2019).

[72] B. Lv, R. Chen, R. J. Li, C. Y. Guan, B. Zhou, G. H. Dong, C. Zhao, Y. C. Li, Y. Wang, H. B. Tao, J. H. Shi, and D. H. Xu, Realization of quasicrystalline quadrupole topological insulators in electrical circuits, Commun. Phys. **4**, 108 (2021).

[73] Y. T. Yang, D. J. Zhu, Z. H. Hang, and Y. D. Chong, Observation of antichiral edge states in a circuit lattice, Sci. China: Phys., Mech. Astron. **64**, 257011 (2021).

[74] J. Wu, X. Q. Huang, Y. T. Yang, W. Y. Deng, J. Y. Lu, W. J. Deng, and Z. Y. Liu, Non-Hermitian second-order topology induced by resistances in electric circuits, Phys. Rev. B **105**, 195127 (2022).

[75] S. Imhof, C. Berger, F. Bayer, J. Brehm, L. W. Molenkamp, T. Kiessling, F. Schindler, C. H. Lee, M. Greiter, T. Neupert, and R. Thomale, Topolectrical-circuit realization of topological corner modes, Nat. Phys. **14**, 925 (2018).

[76] Y. Li, Y. Sun, W. W. Zhu, Z. W. Guo, J. Jiang, T. Kariyado, H. Chen, and X. Hu, Topological LC-circuits based on microstrips and observation of electromagnetic modes with orbital angular momentum, Nat. Commun. **9**, 4598 (2018).

[77] Y. H. Lu, N. Y. Jia, L. Su, C. Owens, G. Juzeliūnas, D. I. Schuster, and J. Simon, Probing the Berry curvature and Fermi arcs of a Weyl circuit, Phys. Rev. B **99**, 020302(R) (2019).

[78] Y. Wang, H. M. Price, B. Zhang, and Y. D. Chong, Circuit implementation of a four-dimensional topological insulator, Nat. Commun. **11**, 2356 (2020).

[79] J. X. Wu, Z. Wang, Y. C. Biao, F. C. Fei, S. Zhang, Z. P. Yin, Y. J. Hu, Z. Y. Song, T. Y. Wu, F. Q. Song, and R. Yu, Non-Abelian gauge fields in circuit systems, Nat. Electron. **5**, 635 (2022).

[80] http://www.linear.com/LTspice.